Discover Materials

Discover

Research

High-density individually addressable platinum nanoelectrodes for biomedical applications

Vidur Raj[1] · Aswani Gopakumar[2] · Gayatri Vaidya[3] · John Scott[4] · Milos Toth[4,5] · Chennupati Jagadish[2,6] · Vini Gautam[7]

Received: 6 April 2022 / Accepted: 1 June 2022
Published online: 13 June 2022

Abstract

3-D vertical nanoelectrode arrays (NEAs) have found applications in several biomedical and sensing applications, including high-resolution neuronal excitation and measurement and single-molecule electrochemical biosensing. There have been several reports on high-density nanoelectrodes in recent years, with the filling ratio of electrodes reaching close to 0.002 (assuming the electrode diameter of 200 nm and pitch of 4 µm). Still, it is well below the nanowire filling ratio required to form interconnected neuronal networks, i.e., more than 0.14 (assuming the electrode diameter of 200 nm and pitch of 1.5 µm). Here, we employ a multi-step, large-area electron beam lithography procedure along with a targeted, focused ion beam based metal deposition technique to realize an individually addressable, 60-channel nanoelectrode chip with a filling ratio as high as 0.16, which is well within the limit required for the formation of interconnected neuronal networks. Moreover, we have designed the NEA chip to be compatible with the commercially available MEA2100-System, which can, in the future, enable the chip to be readily used for obtaining data from individual electrodes. We also perform an in-depth electrochemical impedance spectroscopy characterization to show that the electrochemical behavior and the charge transfer mechanism in the array are significantly influenced by changing the thickness of the SU-8 planarization layer (i.e., the thickness of the exposed platinum surface). In addition to neural signal excitation and measurement, we propose that these NEA chips have the potential for other future applications, such as high-resolution single-molecule level electrochemical and bio-analyte sensing.

Supplementary Information The online version contains supplementary material available at https://doi.org/10.1007/s43939-022-00027-1.

✉ Vidur Raj, vidur.raj@glasgow.ac.uk; ✉ Chennupati Jagadish, chennupati.jagadish@anu.edu.au; ✉ Vini Gautam, vini.gautam@unimelb.edu.au | [1]James Watt School of Engineering, University of Glasgow, University Avenue, Glasgow G12 8QQ, UK. [2]Department of Electronic Materials Engineering, Research School of Physics, The Australian National University, Canberra, ACT 2601, Australia. [3]Australian National Fabrication Facility, Research School of Physics and Engineering, The Australian National University, Canberra, ACT 2601, Australia. [4]School of Mathematical and Physical Sciences, University of Technology Sydney, Ultimo, NSW 2007, Australia. [5]ARC Centre of Excellence for Transformative Meta-Optical Systems (TMOS), University of Technology Sydney, Ultimo, NSW 2007, Australia. [6]ARC Centre of Excellence for Transformative Meta-Optical Systems, Research School of Physics, The Australian National University, Canberra, ACT 2601, Australia. [7]Department of Biomedical Engineering, The University of Melbourne, VIC 3010, Melbourne, Australia.

1 Introduction

Microelectrode arrays (MEAs) are widely accepted in-vitro platforms to study fundamental physiological functions of excitable cells and tissues such as nervous and cardiac tissues/cells [1–3]. Moreover, in recent years, MEAs have also been developed to electrically stimulate these tissues in-vivo with applications targeting the treatment of disorders related to tremors, Parkinson's disease, and dystonia [4]. Deep brain electrical stimulation through surgical implants of micro/nanoelectrodes is already being used to treat various neurological disorders such as essential tremors, Parkinson's disease (PD), and dystonia, which could not generally be treated using the medicine [5]. Other biomedical applications that rely on the electrical stimulation of neuronal tissues include upper and lower limb prostheses for spinal cord injury and stroke; bladder prostheses; cochlear and auditory brainstem implants; visual prostheses for restoration and improvement of vision; and prostheses for stimulation of neurons for epilepsy treatment [6–9]. Deep brain electrical stimulation has also been proposed to treat psychological issues such as depression [4, 10]. In addition to their *in-vivo* application for the treatment of diseases, MEAs have also been indispensable for both *in-vivo* and *in-vitro* electrophysiological and pharmacological study of neuronal cells and tissues [1, 2, 8, 9].

However, commercially available MEAs have certain limitations. The electrode size in MEAs ranges from a few to tens of microns, whereas their pitch can range anywhere from tens to hundreds of microns [3, 11]. In this case, the electrophysiological study of an individual axon or dendrite, simultaneously from more than two intracellular or extracellular sites using MEAs, has been complex due to their smaller diameters, which measure only tens to a few hundred nanometers, and is significantly smaller than MEAs [12, 13]. Although the patch-clamp method can be used to study electrophysiology at a single neuron level, it's often very tedious and can only be used to measure a few neurons at a time [14]. Compared to MEAs, nanoelectrode arrays (NEAs) with diameters within the range of a few hundred nanometers have several advantages as they can enable high-density spatial recordings from multiple points within a neuronal network. Compared to MEAs, NEAs also have reduced ohmic potential drop (because of smaller current due to small size) [15], a decreased time constant (due to reduced double layer capacitance) [11], and an increased signal-to-noise ratio [16]. They are potentially less invasive due to their small size [17, 18]. The high-density nanoelectrode arrays also provide opportunities for longitudinal electrophysiological measurements [18].

Research from our group has recently shown that the isotropic arrangement of a high-density nanowire array can act as physical cues for guiding neurite growth and aid in the formation of a highly interconnected neural network with synchronized synaptic connections [19]. However, the nanowire arrays should be sufficiently dense and closely packed to achieve this with a nanowire array filling ratio (defined in Fig. S1 of supplementary information) of around 0.14. Such a dense array of individually addressable nanoelectrode can significantly enhance the understanding of highly correlated signal propagation amongst the neuronal network. Although there have been previous reports on individually addressable nanoelectrode arrays [14, 18], the nanowire array filling ratio remained below 0.002, which is substantially lower than those required to achieve correlated firing of neurons. Therefore, for this particular study, we aimed to fabricate a nanoelectrode array exceeding the minimum filling ratio of nanowires required to achieve the highly correlated function of in-vitro neurons based on our earlier findings [19]. Here, we choose platinum as the electrode material because of its high biocompatibility and low impedance [20], and having been successfully established as working electrodes in Cochlear implants [21].

Here, we report the fabrication and electrochemical characterization of individually addressable nanoelectrode arrays for application in neuroscience. We achieve the highest reported filling ratio of 3D platinum nanoelectrodes, which is expected to assist in the in-vitro growth of highly interconnected neural networks and simultaneously allow for high-resolution spatio-temporal characterization of the neuronal signals down to single neurons. Another critical feature of our NEAs is that we have performed all the fabrication steps at relatively low temperatures, meaning that a similar process can be extended for the fabrication of NEAs on flexible substrates.

2 Experimental details

The nanoelectrode array (NEA) fabrication started with piranha cleaning of intrinsic silicon (100) substrate with resistivity exceeding 1000 Ω-cm. The piranha cleaning can also be substituted by oxygen plasma etching followed by a 2 min dip in 1% HF. Subsequently, the silicon substrate was spin-coated with bi-layer PMMA coating consisting

of a layer of 2% of 495 k PMMA dissolved in anisole followed by a layer of 4% PMMA dissolved in PMMA. Both the layers were coated at 4000 rpm for 45 s without ramping, and the total resist thickness was approximately 280 nm. A bi-layer coating was used to facilitate the metal lift-off. Subsequently, the sample with PMMA was transferred to RAITH150 TWO for e-beam lithography (EBL). A specifically designed EBL procedure was used to fabricate a large-area nanoelectrode array with high resolution and minimum stitching error. A two-level EBL was performed to write more coarse structure and alignment markers in the first instance, followed by the writing of smaller features. The paper's results and discussion section provide more details about the EBL procedure. After EBL, the sample was developed in a 3:1 ratio of IPA: Water under constant sonication for 2 min 10 s. Subsequently, a 20 nm Ti/100 nm Au was deposited by e-beam evaporation and lifted off by leaving the sample in acetone for at least two hours at room temperature.

After the metal lift-off, the sample only contained alignment markers and smaller features written by EBL. Next, photolithography was used to connect the EBL-defined patterns with larger metal connectors (for details, see supplementary information Fig. S1). Before photolithography, the substrate was cleaned in acetone and IPA followed by DI water under sonication for 2 min each to remove any contamination residue from the EBL and lift-off processing of the sample. Next, the sample was baked at 180 °C for 2 min to remove any water and organic residue left after cleaning. Next, the substrate was coated with MaN-2405 negative resist spin-coated at 4000 RPM for photolithography for 45 s. Subsequently, the sample was baked at 90 °C for 90 s. The substrate was exposed under UV light, followed by the development of the exposed pattern for 90 s in MaD 332. Next, the same 20 Ti/100 nm Au thin film was deposited using e-beam evaporation followed by lift-off in acetone at room temperature.

The chip with 2D metal electrode formed by EBL and photolithography was then used for deposition of 3D platinum nanoelectrode using focused ion beam (FIB) and focused electron beam (FEB) based platinum deposition. We used trimethyl(methylcyclopentadienyl)-platinum(IV) as the precursor for both FIB and FEB induced platinum depositions. The FEB induced Pt deposition was done in Helios G4 PFIB DualBeam microscope, where FIB based Pt deposition used a FEI Helios 600 Nanolab system. The nanopillars were grown individually on each of the 2D metal pads. The precursor was locally supplied using a gas injection system positioned 200 µm above the sample surface. The electron beam energy and current were fixed at 20 kV and 400 pA, respectively, whereas, defocus of 30 µm was used. At the same time, FIB deposition was carried out using ion beam energy and current of 30 kV and 9.7 pA, respectively.

3 Results and discussion

3.1 Fabrication

The fabrication of nanoelectrode arrays started with the fabrication of metal pads connecting the nanoelectrodes. The metal pads specifications for reading the output signal from nanoelectrodes were matched explicitly to a 60-electrode microelectrode array chip of multichannelsystems (MCS GmbH). It consists of 60 individually addressable square metal pads of 2.2 mm × 2.2 mm separated by 150 µm (see supplementary information Fig. S2). In the future, it should be possible to obtain a signal from nanoelectrodes through these metal pads using the MEA2100 overhead stage (see supplementary information Fig. S2).

In our 3-D NEA, the total area written by EBL exceeds 5 mm^2, and the dimension of structure varies from 20 µm down to tens of nanometers. Therefore, we needed to achieve sufficiently fast electron-beam lithography while maintaining high resolution. To achieve it, we divided the EBL area into three regions based on the minimum feature size that is to be written, and during EBL patterning, we used a 30 µm aperture for smaller feature sizes, whereas, for medium and large size patterns, we used 60 µm and 120 µm apertures, respectively. A complete schematic of the process is shown in Fig. S3 of supplementary information. In conventional EBL systems, aperture sizes are directly related to the beam current, which in turn controls the writing speed of EBL, as explained in Eq. (1) [22].

$$T_{single\ pixel} \approx \frac{Dose * Area^2}{Beam\ Current} \tag{1}$$

In the above equation, $Dose$ is defined as the clearance dose of the resist (given in terms of µC/cm^2), $Area$ is the total area to be exposed (given in terms of cm^2), and the $Beam\ Current$ is the current of the electron beam (given in terms of nA). Please note that in Eq. 1, the stage movement and settling time have not been taken into account, as we individually define these parameters for every aperture (i.e., beam current). Figure 1a shows an after-metal lift-off optical micrograph of the total area written by EBL. Regions with smaller structures written by 30 µm and

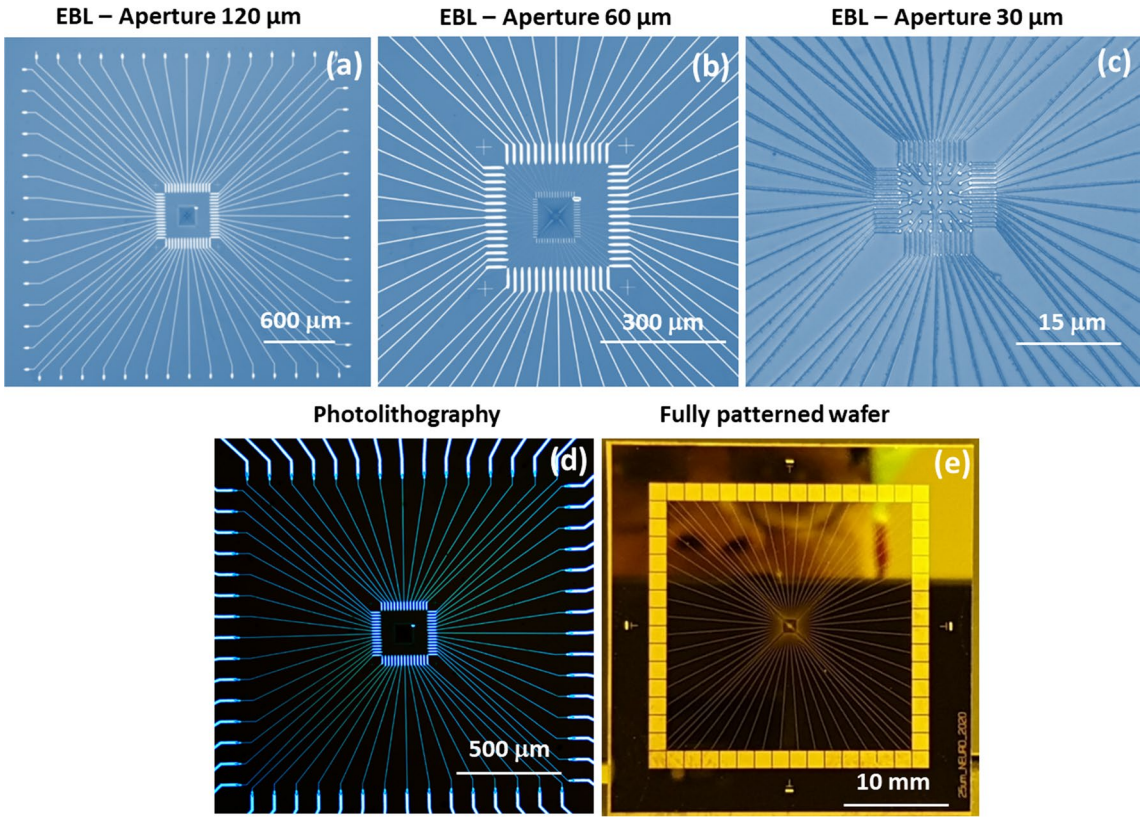

Fig. 1 **a**–**c** shows optical microscope (false-colored) images of the pattern written by EBL (after metal lift-off). More than 20 µm thick lines were written by 120 µm aperture, whereas lines less than 1 µm were written by 60 µm aperture, and lines less than 200 nm were written by 30 µm aperture. **d** Using alignment markers written by EBL, a near-perfect alignment between EBL and photolithography patterns can be obtained. **e** A fully patterned wafer with nanoelectrode arrays

60 µm apertures are shown in Fig. 1b and c. During EBL, four alignment markers were also written (shown in a red circle in Fig. S2 of supplementary information) using 120 µm aperture to align the photolithography pattern with EBL exposed area. Figure 1d shows the alignment of EBL patterns with photolithographically defined patterns after metal lift-off. A fully patterned wafer with gold metal electrodes on a silicon substrate is shown in Fig. 1e.

Furthermore, to fabricate 3D nanoelectrodes, we use focused ion beam (FIB), and focused electron beam (FEB) based platinum deposition techniques. Although the platinum deposited by FEB was smoother and more conductive than the FIB deposited platinum, the backscattering from the electron beam was higher than the ion beam leading to shorting of electrodes due to the deposition of a thin platinum film all-around 3D electrodes (See supplementary Fig. S4). The unequal distribution of nanoelectrodes is mainly due to beam and stage drift over time, and it's not unusual for the exposed area to drift moderately in time scales of minutes (due to ambient noise or focused beam instability), leading to slight displacement in the nanowire position. Figure 2a shows a scanning electron microscope (SEM) image of circular gold nano pads of 2D nanoelectrode. The platinum nanoelectrodes were deposited individually at this predefined array of circular gold pads. Figure 2b and c respectively show the top and tilted SEM images of 3D platinum nanoelectrodes deposited by FIB. The top diameters of nanoelectrodes were approximately 350 nm, whereas the bottom diameter of the nanowire was around 550 nm giving it a conical shape. The calculated filling ratio using these parameters comes out to be 0.16, which is very similar to what is required for achieving a highly interconnected neural network. Finally, a SU-8 thin film planarization technique was used to isolate these electrodes from each other, as discussed in reference[23]. A further increase in filling factor can be achieved by optimizing the FIB and FEB depositions to achieve near cylindrical nanoelectrodes.

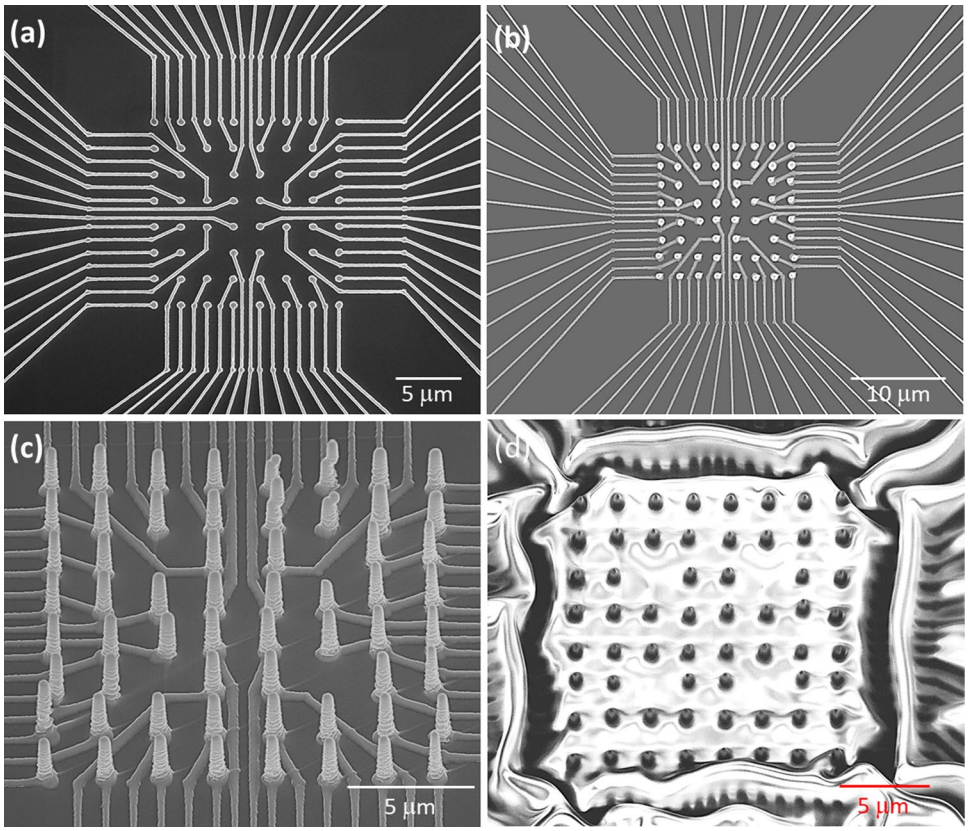

Fig. 2 **a** SEM image of circular gold nano pads on which 3D platinum nanowires were deposited using FIB and FEB-based platinum deposition technique; **b** and **c** respectively shows the top and tilted SEM views of platinum nanowires deposited by FIB. **d** SEM of nanoelectrode array separated from each other using SU-8. Using different SU-8 etching times, different lengths of the platinum nanowire can be exposed, which controls the electrochemical charge transfer in these electrodes

3.2 Electrochemical impedance spectroscopy (EIS) measurement

A nanoelectrode can be understood as a circuit element mediating the charge transfer from an electronic conductor to an ionic conductor, and the electrochemical impedance spectroscopy (EIS) provides information about the effectiveness and mechanism of this charge transfer, making it one of the primary measurements required to assess the quality of nanoelectrodes. Also, a neural signal is distributed over a range of frequencies corresponding to different neural processes. For example, local field potentials signifying synaptic activity are contained in the low-frequency band (i.e., approximately 1–250 Hz), whereas individual neuronal spikes fall in a relatively high-frequency range (i.e., around 500–3000 Hz) [24]. This makes it essential to study the EIS over a range of frequencies, and in our case, we perform EIS measurements for 0.1–10^5 Hz.

To ensure that we only obtain electrochemical measurement data from 3D nanoelectrodes, we employ several levels of epoxy and polymer coatings to eliminate any contribution from silicon substrate or gold wire connecting the nanoelectrodes, as shown in Fig. 3a. To prepare the substrate for EIS measurements, we uniformly cover the back of the silicon substrate using epoxy tape just after platinum metal deposition. It covers the back of the silicon substrate and the edges of the silicon. Thereafter, a 250 nm thick film of PMMA is spin-coated to isolate the gold wire connecting the nanoelectrodes. The choice of PMMA was based on the fact that it can be dissolved in acetone to expose the gold contact, but it does not dissolve in IPA or methanol, and therefore they can be used for cleaning substrates before measurement. Subsequently, a SU-8 layer was deposited over a small area (not covering the gold metal pads) to isolate the 3D nanoelectrodes. To remove polymers coated on the surface of platinum nanoelectrodes, we use an alternate step of oxygen plasma cleaning followed by oxide removal in a highly diluted HF (1:50 HF:Water), as detailed in reference [23]. We confirm the complete removal of SU-8 using SEM, as already shown in Fig. 2d. Finally, the SU-8 is cured to form a hard contact between the nanoelectrodes that cannot readily dissolve in organic solvents. Each gold contact was individually exposed during the measurement of nanoelectrodes, ensuring no contribution from any other gold contact connecting the 3D nanoelectrodes. Moreover, to study nanoelectrodes' length-dependent EIS behavior, we control the thickness of SU8 by etching it for different durations in the presence of dense oxygen plasma before its curing.

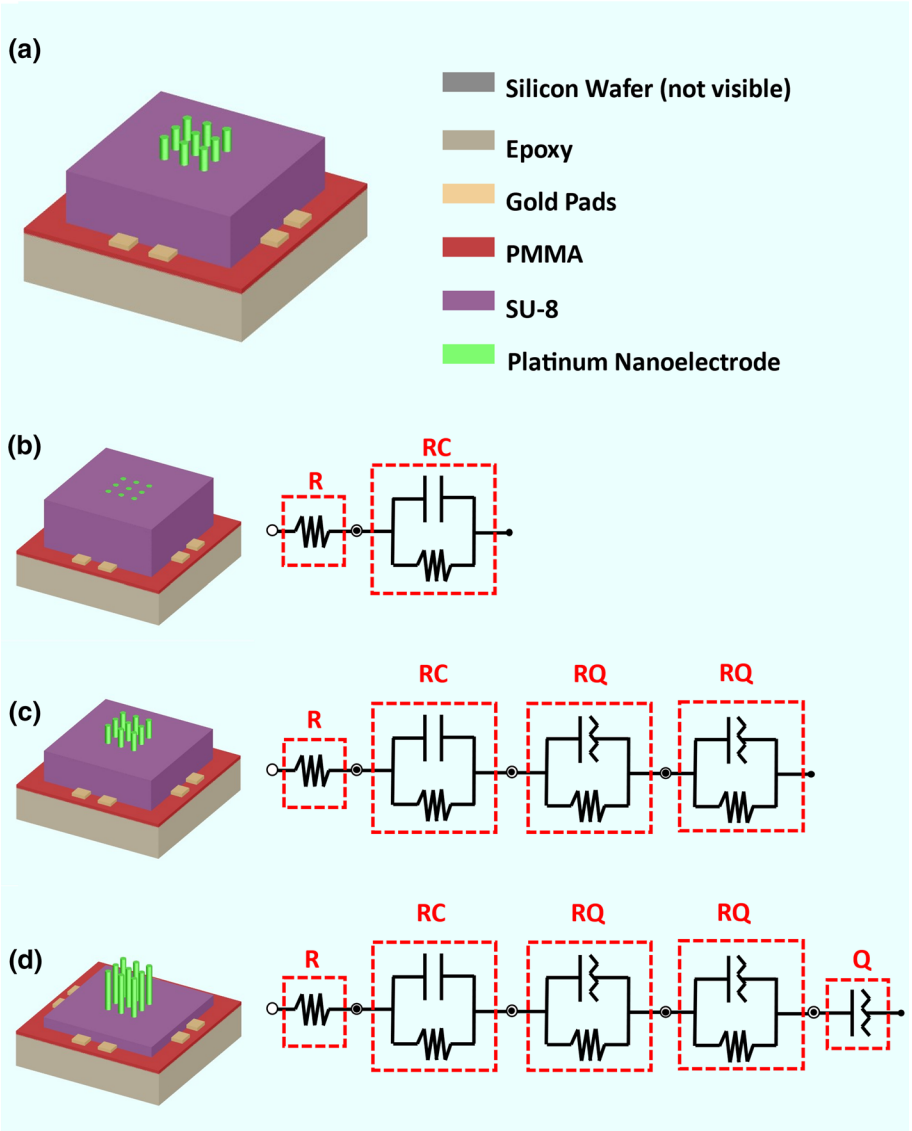

Fig. 3 **a** 3D schematic of an NEA chip ready for electrochemical measurements. It consists of an epoxy layer that completely isolates the back and side of the silicon wafer on which the nanoelectrodes are defined. The nanoelectrodes and metal contact pads are electrically isolated from each other through a bi-layer polymer consisting of PMMA and SU-8. PMMA is chosen because it can be removed in IPA during measurement of individual gold contact and its extremely low sensitivity to UV exposure, which allows for selective curing of SU-8. Finally, different lengths of platinum nanowires can be exposed by etching the SU-8 (before curing) for different lengths of time. **b** Sample 1: Schematic showing NEA with only the tip of the platinum nanowire exposed, and a corresponding circuit used for fitting EIS data is shown alongside. **c** Sample 2: Schematic showing NEA with approximately 500 nm of the platinum nanowire exposed and alongside is shown a corresponding circuit used for fitting EIS data. **d** Sample 3: Schematic showing NEA with approximately 1 µm of the platinum nanowire exposed and a corresponding circuit used for fitting EIS data is shown alongside

Moreover, before fitting the EIS data to explain the charge transfer mechanisms, we check the measured data against the Kramers–Kronig (K–K) relation to ascertain its quality [25]. The K–K relation connects the real and imaginary parts of a complex function and is a measure of linearity, stability, and casualty of the system. The system's linearity means that the response is linear and perturbation is small; stability of the system means that it does not change with time (for the duration of measurement), whereas casualty implies that the measured response is only due to the excitation signal. The check against the K–K model is performed using a built-in command in the NOVA software (obtained from Autolab Instruments) that is based on the work presented in reference [26]. In short, during K–K model fitting, the data is fitted against a circuit that always satisfies the K–K assumptions. In NOVA software, this circuit consists of a series of RC circuits equal to the number of measured data points, and the quality of data is measured in terms of χ^2_{ps} (pseudo chi-squared fit value) given by Eq. (2).

$$\chi^2_{ps} = \sum_{i=1}^{n} \frac{[Z_{re,i} - Z_{re}(\omega_i)] - [Z_{im,i} - Z_{im}(\omega_i)]}{|Z(\omega_i)|} \tag{2}$$

where, $Z_{re,i}$ and $Z_{im,i}$ are the measured real and imaginary parts of impedance, $Z_{re}(\omega_i)$ and $Z_{im}(\omega_i)$ are the real and imaginary parts of impedance simulated as a function of the radial frequency ω_i, and $|Z(\omega_i)|$ is the vector length (absolute value) of the modeling function. The lower is the χ^2_{ps}, the higher is the data quality, and vice-versa. In our case, for all presented data, the χ^2_{ps} was between 10^{-3} and 10^{-4}, and the χ^2_{ps} reduced below 10^{-5} if the data points are restricted to

frequencies more than 10 Hz. The data quality in the future can further be improved by employing a 2- or 4-electrode measurement, which reduces the contribution of uncertainties induced by the reference electrode. Also, high-quality wire bonding or soldering can be investigated instead of crocodile/alligator clips for applying and reading the current through electrodes.

After confirming the quality and reliability of EIS data, we moved on to fitting the Nyquist and Bode plots. Here onwards, for the sake of discussion, we categorize our samples into samples 1–3 depending on the thickness of platinum nanowire exposed (for details, see Figure caption of Fig. 3b–d). Figure 3b–d shows equivalent circuit models along with a figurative representation for nanoelectrodes with varying thicknesses of SU-8, whereas Fig. 4a–c shows the corresponding fitting of Nyquist and Bode plots. Additionally, from here onwards, we use R, C, Q, RC, and RQ to respectively represent the resistor, the capacitor, the constant phase element, the capacitor in parallel to resistors, and the constant phase element in parallel to the resistor. Also, R_{elec} denote the resistance due to electrolyte, R_{ct} denote charge transfer resistances, C_{pt} denotes platinum nanoelectrode capacitance at the electrode/electrolyte interface, and Q_{pt} indicates the constant phase element representing the non-ideal capacitive behavior of platinum nanoelectrode.

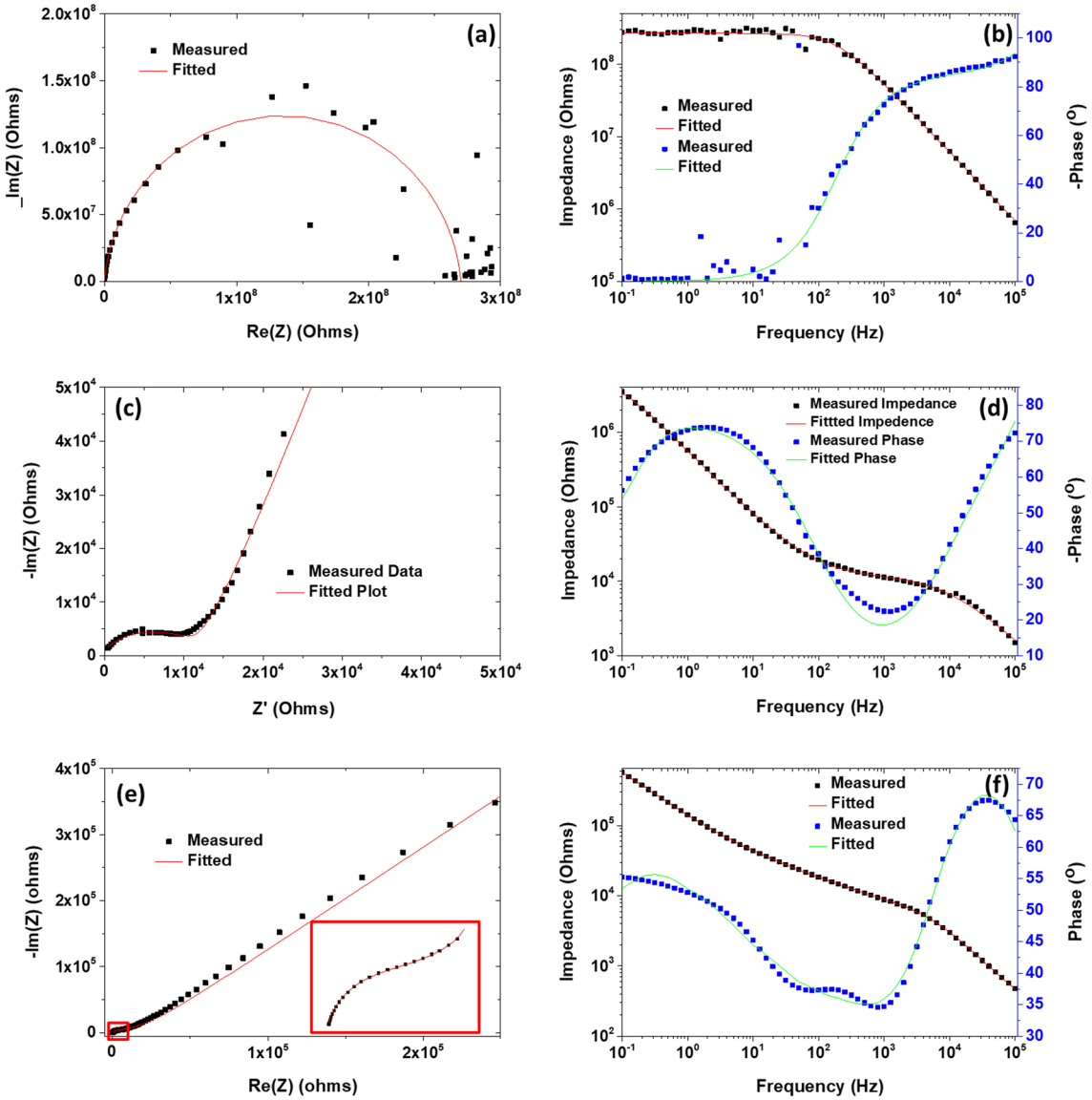

Fig. 4 **a** and **b** shows the fitted Nyquist and Bode plots for Sample 1; **c** and **d** shows the fitted Nyquist and Bode plots for Sample 2; **e** and **f** shows the fitted Nyquist and Bode plots for Sample 3

It's apparent from the fitting of Nyquist and Bode plots that there is a significant shift in the impedance spectra as a function of SU-8 etching time (i.e., the thickness of platinum nanowire). For example, for sample 1, where only the tip of platinum nanoelectrode is exposed. An SEM image of platinum nanoelectrode with only tip exposed is shown in Fig. S3(e), (f). The Nyquist and Bode plots can be fitted by a relatively simple circuit consisting of a resistor (R_{elec}) in series connection with R_{ct} and C_{ct} in parallel, giving an almost perfect semi-circle in the Nyquist plot. As expected, because a very small portion of the electrode is exposed, the impedance is very high and exceeds more than 10^6 Ω for almost all measured frequency region, and more than 10^8 Ω for smaller frequency ranges. A high charge transfer resistance and low capacitance of ~ 260 MΩ and 3 pF signify that the impedance originates from the double charge layer formation at the nanoelectrode/electrolyte for most frequency ranges. A more clear picture is obtained by analyzing the phase *vs.* frequency Bode plot, which shows that C_{pt} is low only at sufficiently higher frequencies; however, as the frequency drops, the impedance corresponding to C_{pt} increases, and most current flow through the resistor.

In comparison to sample 1, sample 2 (see Fig. 3c) has very different EIS characteristics and requires a more complex circuit to explain the Nyquist and Bode's plots shown in Fig. 4b. The circuit presented in Fig. 3c consists of R_{elec} connected in series with one RC component and 2 RQ components. The magnitude of the capacitive element for sample 2 is several hundred nF, suggesting an increased surface area of the tip of the nanoelectrodes. At the same time, the requirement of constant phase element for fitting points to the polycrystalline and rough radial surface of platinum nanoelectrode, which is also evident in the SEM images shown in Fig. 2 [27, 28] The constant phase element is frequently used to model an imperfect capacitor, and its impedance (Z_{cpe}) is given by:

$$Z_{cpe} = \frac{1}{Q_0 \cdot (i \cdot \omega)^n} \tag{3}$$

In the above equation, Q_0 and n are frequency-dependent parameters, defined such that $Q_0 = 1/|Z_{cpe}|$ at $\omega = 1 rad/s$, and phase is always $-(90.n)°$ with $0 \leq n \leq 1$. Therefore, an ideal capacitor is when $n = 1$. In the current case, the parameter n for both the RQ elements is near to 1 for shorter nanoelectrodes (~ 200 nm) and decreases to 0.6–0.7 for longer nanoelectrodes (~ 500 nm). The roughness of nanoelectrode also increases the effective surface area of the nanoelectrode, which can also explain almost an exponential decrease in impedance of nanoelectrodes with a linear increase in the thickness of platinum nanoelectrodes. We also postulate that although one of the RQ elements represents the polarization of the radial surface of nanoelectrode due to applied sinusoidal potential, the other RQ element might be due to the secondary polarization of nanoelectrodes adjacent to the original electrode where the potential is applied. We measured more than five different samples, and we see similar behavior that an additional RQ element (to account for secondary polarization) is required to achieve fitting of EIS data when there are more than a few hundred nanometers of nanoelectrode is exposed. Another important clue that the second RQ element must represent secondary polarization is that the polarization resistance corresponding to secondary polarization is significantly high and is of the order of MΩ to TΩ, whereas the polarization resistance of the primary electrode is only a few kΩ. Also, increasing the number of this element significantly improves the fitting parameter of EIS data. This may be because a single lump sum RQ element is not sufficient to achieve a high-quality fit. There are several nanoelectrodes near the primary electrode (i.e., electrode to which potential is applied), and each needs to be fitted by an individual RQ element because of their nonuniformity. Nonetheless, even with 1 RC and 2RQ in series with R_{elec}, χ^2 (fitting parameter) of ~ 0.1 can be achieved. Here, we would also like to mention that except for sample 1, the fitting of EIS for all other samples significantly improved by increasing the number of RQ elements. Still, we have tried to minimize the number of fitting elements to explain the results better and give readers a clearer view of the charge transfer mechanism in these nanoelectrodes. In the future, it would be interesting to see how does the spacing between the electrodes influence the secondary polarization because so far, such a study has not been attempted.

During our fabrication, we also found cases where nanoelectrodes were shorted with each other, most probably during platinum deposition. In this case, there is a steep drop in the impedance with increasing frequency (see supplementary Fig. S5(a) and (b)), which might be due to the simultaneous polarization of two electrodes. Although, even in this case, EIS can be reliably fitted with 1 RC and 2RQ in series with R_{elec}, there are subtle differences in the Bode plot of sample 2, as should be evident by comparing Fig. 4c and d, with supplementary information Fig. S5(a) and (b). For platinum deposited by electron beam, almost all nanoelectrodes showed shorting behavior as shown in supplementary information Fig. S5(c) and (d).

Sample 3 EIS data can be fitted with a very similar circuit to sample 2, except that now there is another constant phase element in series with the R_{elec}, and 1RC and 2RQ elements, as shown in Fig. 3d. The origin of 1RC and 2RQ elements is very similar to samples 2, whereas the origin of an additional constant phase element in series can be

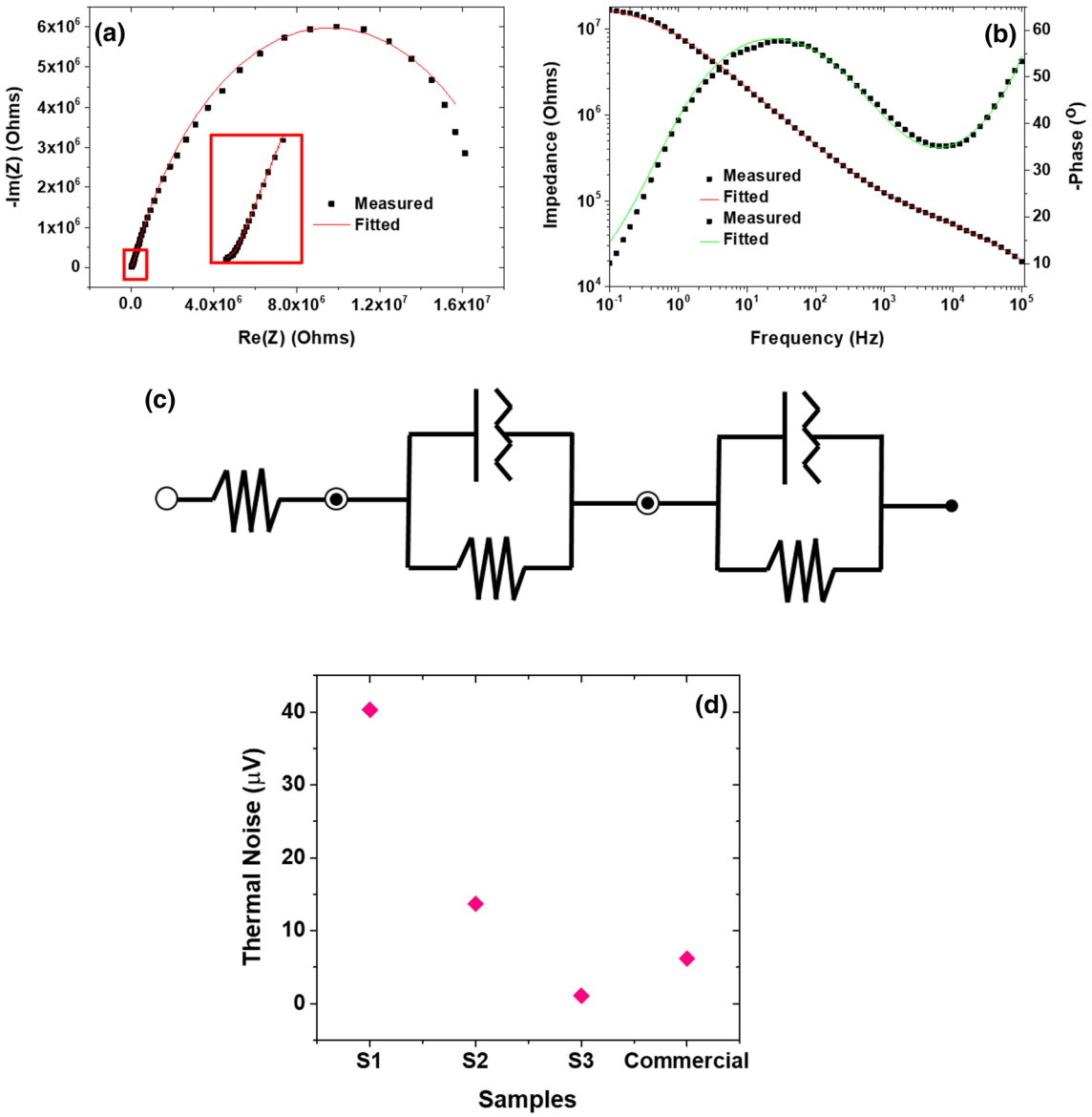

Fig. 5 **a** and **b** respectively shows the Nyquist and Bode plots for one of the electrodes of 2D microelectrode purchased from Multichannelsystems. **c** A corresponding circuit diagram used for fitting of the data shown in **a** and **b**

explained by sufficient thinning of SU-8. When SU-8 thickness is sufficiently reduced, a double layer will be formed near the electrolyte/SU8/gold contact interface, which is explained by an additional constant phase element in series.

Nevertheless, the EIS of sample 2 is very similar to that of commercial MEAs (see Fig. 5a–c), showing the usefulness of a 3D NEA. The commercial MEAs were obtained from multichannelsystems and had the product code: 60EcoMEA-w/o. Our results indicate that even though NEAs have a small size compared to MEAs, they can still reach a very similar impedance to MEAs and offer a very similar charge transfer mechanism, as apparent from both Nyquist and Bode plots. One of the significant differences between NEAs and MEAs is the lack of secondary polarization in the case of MEAs. This is understandable considering the electrodes in the case of MEAs are significantly further apart compared to NEAs. Also, the rough top surface explains the lack of RC components and the presence of RQ elements.

Finally, one of the primary reasons for performing EIS measurements is to estimate the electrode–electrolyte interface noise, which is mainly controlled by thermal noise at frequencies higher than 10 Hz [9, 29]. The corresponding equivalent thermal noise for nanoelectrodes can be estimated by Eq. (4):

$$V_{th} = \sqrt{4 \cdot k \cdot T \cdot Re(Z) \cdot \nabla f} \tag{4}$$

In the above equation, k is the Boltzman's constant, T is the absolute temperature, $Re(Z)$ is the real component of the electrode impedance, and ∇f is the frequency bandwidth. Figure 5d shows the calculated thermal noise for samples 1–3 in comparison to the commercial electrodes. As expected, thermal noise decreases with decreasing impedance, and in the NEAs, the thermal noise is directly related to the thickness of platinum nanoelectrode exposed to the electrolyte. Also, for sample 3, where almost more than half of platinum nanoelectrode is exposed, thermal noise reduces to as low as ~ 1 µV. We believe such a low impedance and resulting low thermal noise, in the case of NEAs, is a result of the high surface roughness of platinum nanoelectrode deposited using a focused ion beam.

4 Future work

In the future, it would be interesting to study how FIB parameters can be used to fine-tune the electrochemical properties of these nanoelectrodes further and improve the impedance and thermal noise. It would also be interesting to study the effect of packaging density on the electrochemical behavior of NEAs, effectively to understand the origin of secondary polarization terms (as appeared in our sample 2 and sample 3). In addition, given that the whole process described in this paper was performed at a low temperature (< 200 °C), in the future, it may be possible to fabricate NEAs on flexible and transparent substrates, which will be substantially more useful than NEAs on silicon, especially for neuroscience applications. However, one of our immediate goals is to increase nanoelectrodes density and test presented NEAs against in-vitro neuronal networks for their stimulation and signal measurement.

The NEAs fabrication methods presented in the paper provide a straightforward way of achieving a high-density nanoelectrode array with low impedance for a wide range of frequencies. This, in turn, extends NEAs application from neuroscience to high-resolution single-molecule level electrochemical and bio-analyte sensing. For example, high density individually addressable nanoelectrode has previously been shown to significantly improve the sensitivity, selectivity, and unlabeled detection of bio- and chemical species [30, 31]. An improvement in sensing with high-density nanoelectrodes is mainly achieved due to their large active surface area and high surface permeability [32], and significantly reduced interaction volume [33], which improves the interaction of biological and chemical entities with the nanoelectrodes.

5 Conclusions

In conclusion, this paper presents the fabrication of high-density individually addressable 3D platinum nanoelectrodes formed by focused-ion beam and electron-beam lithography. An in-depth analysis of EIS shows that sufficiently low impedance can be achieved for these nanoelectrodes by exposing just a few hundred nanometers of platinum nanoelectrodes, whereas by exposing more than one micron of nanoelectrode, an impedance less than 10^4 ohms can be achieved. As a result, the thermal noise corresponding to these nanoelectrodes can be significantly reduced by controlling the thickness of the nanoelectrode exposed, and thermal noise of ~ 1 µV can be achieved for NEAs with more than 1 µm of exposed platinum nanoelectrode. Moreover, the behavior of these nanoelectrodes is compared against a commercially available MEA, and it is shown that their electrochemical performance is comparable to commercially available MEAs. Finally, we discuss the future work and briefly discuss the presented NEAs for applications beyond neuronal stimulation and measurement.

Acknowledgements Dementia Australia Research Foundation (DARF) and Yulgilbar Foundation are gratefully acknowledged for their financial support. Dr. Gautam also acknowledges the support from the Australian Research Council's Discovery Early Career Researcher Award DE180100775. Access to the fabrication facilities is made possible through the Australian National Fabrication Facility, ACT Node.

Author contributions VG and CJ designed and managed the project. VR wrote the manuscript and did all the experiments. AG, GV, JS, and MT helped with the fabrication of nanoelectrodes. All authors reviewed the manuscript. All authors read and approved the final manuscript.

Data availability The datasets generated during and/or analyzed during the current study are available from the corresponding author on reasonable request.

Declarations

Competing interests The authors declare that they have no competing financial interests.

References

1. Spira ME, et al. Multi-electrode array technologies for neuroscience and cardiology. Nat Nanotechnol. 2013;8(2):83–94. https://doi.org/10.1038/nnano.2012.265.
2. Stett A, et al. Biological application of microelectrode arrays in drug discovery and basic research. Anal Bioanal Chem. 2003;377(3):486–95. https://doi.org/10.1007/s00216-003-2149-x.
3. Szunerits S, et al. 10—microelectrode arrays. In: Zoski CG, editor., et al., Handbook of electrochemistry. Elsevier: Amsterdam; 2007. p. 391–428. https://doi.org/10.1016/B978-044451958-0.50023-9.
4. Mayberg HS, et al. Deep brain stimulation for treatment-resistant depression. Neuron. 2005;45(5):651–60. https://doi.org/10.1016/j.neuron.2005.02.014.
5. Lozano AM, et al. Deep brain stimulation: current challenges and future directions. Nat Rev Neurol. 2019;15(3):148–60. https://doi.org/10.1038/s41582-018-0128-2.
6. Gulino M, et al. Tissue response to neural implants: the use of model systems toward new design solutions of implantable microelectrodes. Front Neurosci. 2019. https://doi.org/10.3389/fnins.2019.00689.
7. Parastarfeizabadi M, et al. Advances in closed-loop deep brain stimulation devices. J Neuroeng Rehabil. 2017;14(1):79. https://doi.org/10.1186/s12984-017-0295-1.
8. Hong G, et al. Novel electrode technologies for neural recordings. Nat Rev Neurosci. 2019;20(6):330–45. https://doi.org/10.1038/s41583-019-0140-6.
9. Obien MEJ, et al. Revealing neuronal function through microelectrode array recordings. Front Neurosci. 2015. https://doi.org/10.3389/fnins.2014.00423.
10. McCreery DB, et al. A characterization of the effects on neuronal excitability due to prolonged microstimulation with chronically implanted microelectrodes. IEEE Trans Biomed Eng. 1997;44(10):931–9. https://doi.org/10.1109/10.634645.
11. Liu Y, et al. Micro/nano electrode array sensors: advances in fabrication and emerging applications in bioanalysis. Front Chem. 2020. https://doi.org/10.3389/fchem.2020.573865.
12. Bakkum DJ, et al. Tracking axonal action potential propagation on a high-density microelectrode array across hundreds of sites. Nat Commun. 2013;4(1):2181. https://doi.org/10.1038/ncomms3181.
13. Debanne D, et al. Axon physiology. Physiol Rev. 2011;91(2):555–602. https://doi.org/10.1152/physrev.00048.2009.
14. Abbott J, et al. A nanoelectrode array for obtaining intracellular recordings from thousands of connected neurons. Nat Biomed Eng. 2020;4(2):232–41. https://doi.org/10.1038/s41551-019-0455-7.
15. Arrigan DWM. Chapter 2—nanoelectrode arrays for electroanalysis. In: Wain AJ, Dickinson EJF, editors. Frontiers of nanoscience. Elsevier: Amsterdam; 2021. p. 49–86. https://doi.org/10.1016/B978-0-12-820055-1.00006-X.
16. Schmueser I, et al. A systematic study of the influence of nanoelectrode dimensions on electrode performance and the implications for electroanalysis and sensing. Faraday Discuss. 2013;164:295–314. https://doi.org/10.1039/C3FD00038A.
17. Gällentoft L, et al. Size-dependent long-term tissue response to biostable nanowires in the brain. Biomaterials. 2015;42:172–83. https://doi.org/10.1016/j.biomaterials.2014.11.051.
18. Liu R, et al. High density individually addressable nanowire arrays record intracellular activity from primary rodent and human stem cell derived neurons. Nano Lett. 2017;17(5):2757–64. https://doi.org/10.1021/acs.nanolett.6b04752.
19. Gautam V, et al. Engineering highly interconnected neuronal networks on nanowire scaffolds. Nano Lett. 2017;17(6):3369–75. https://doi.org/10.1021/acs.nanolett.6b05288.
20. Donaldson ND, et al. When are actively balanced biphasic ('Lilly') stimulating pulses necessary in a neurological prosthesis? I. Historical background; Pt resting potential, Q studies. Med Biol Eng Comput. 1986;24(1):41–9. https://doi.org/10.1007/bf02441604.
21. Tykocinski M, et al. Chronic electrical stimulation of the auditory nerve using high surface area (HiQ) platinum electrodes. Hear Res. 2001;159(1):53–68. https://doi.org/10.1016/S0378-5955(01)00320-3.
22. Greve MM, et al. Optimization of an electron beam lithography instrument for fast, large area writing at 10 kV acceleration voltage. J Vac Sci Technol B. 2013;31(4): 043202. https://doi.org/10.1116/1.4813325.
23. Raj V, et al. High-efficiency solar cells from extremely low minority carrier lifetime substrates using radial junction nanowire architecture. ACS Nano. 2019;13(10):12015–23. https://doi.org/10.1021/acsnano.9b06226.
24. Buzsáki G, et al. The origin of extracellular fields and currents—EEG ECoG, LFP and spikes. Nat Rev Neurosci. 2012;13(6):407–20. https://doi.org/10.1038/nrn3241.
25. Vadhva P, et al. Electrochemical impedance spectroscopy for all-solid-state batteries: theory methods and future outlook. ChemElectroChem. 2021;8(11):1930–47. https://doi.org/10.1002/celc.202100108.

26. Boukamp BA. A linear Kronig–Kramers transform test for immittance data validation. J Electrochem Soc. 1995;142(6):1885–94. https://doi.org/10.1149/1.2044210.
27. Kim C-H, et al. An investigation of the capacitance dispersion on the fractal carbon electrode with edge and basal orientations. Electrochim Acta. 2003;48(23):3455–63. https://doi.org/10.1016/S0013-4686(03)00464-X.
28. Mulder WH, et al. Tafel current at fractal electrodes: connection with admittance spectra. J Electroanal Chem Interfacial Electrochem. 1990;285(1):103–15. https://doi.org/10.1016/0022-0728(90)87113-X.
29. Heer F, et al. CMOS microelectrode array for the monitoring of electrogenic cells. Biosens Bioelectron. 2004;20(2):358–66. https://doi.org/10.1016/j.bios.2004.02.006.
30. Drummond TG, et al. Electrochemical DNA sensors. Nat Biotechnol. 2003;21(10):1192–9. https://doi.org/10.1038/nbt873.
31. Zhang J, et al. Localized electrochemiluminescence from nanoneedle electrodes for very-high-density electrochemical sensing. Anal Chem. 2017;89(21):11399–404. https://doi.org/10.1021/acs.analchem.7b02363.
32. Abdel-Karim R, et al. Review—nanostructured materials-based nanosensors. J Electrochem Soc. 2020;167(3): 037554. https://doi.org/10.1149/1945-7111/ab67aa.
33. Kim D-S, et al. Electrochemical detection of dopamine using periodic cylindrical gold nanoelectrode arrays. Sci Rep. 2018;8(1):14049. https://doi.org/10.1038/s41598-018-32477-0.